ACS NANO

www.acsnano.org

ARTICLE

Organosilicon-Based Ligand Design for High-Performance Perovskite Nanocrystal Films for Color Conversion and X-ray Imaging

Junchi Chen, Guocan Jiang,* Elias Hamann, Henning Mescher, Qihao Jin, Isabel Allegro, Philipp Brenner, Zhengquan Li, Nikolai Gaponik, Alexander Eychmüller, and Uli Lemmer*

Cite This: *ACS Nano* 2024, 18, 10054−10062

Read Online

ACCESS | Metrics & More | Article Recommendations | Supporting Information

ABSTRACT: **Perovskite nanocrystals (PNCs) bear a huge potential for widespread applications, such as color conversion, X-ray scintillators, and active laser media. However, the poor intrinsic stability and high susceptibility to environmental stimuli including moisture and oxygen have become bottlenecks of PNC materials for commercialization. Appropriate barrier material design can efficiently improve the stability of the PNCs. Particularly, the strategy for packaging PNCs in organosilicon matrixes can integrate the advantages of inorganic-oxide-based and polymer-based encapsulation routes. However, the inert long-carbon-chain ligands (e.g., oleic acid, oleylamine) used in the current ligand systems for silicon-based encapsulation are detrimental to the cross-linking of the organosilicon matrix, resulting in performance deficiencies in the nanocrystal films, such as low transparency and large surface roughness. Herein, we propose a dual-organosilicon ligand system consisting of (3-aminopropyl)triethoxysilane (APTES) and (3-aminopropyl)-triethoxysilane with pentanedioic anhydride (APTES-PA), to replace the inert long-carbon-chain ligands for improving the performance of organosilicon-coated PNC films. As a result, strongly fluorescent PNC films prepared by a facile solution-casting method demonstrate high transparency and reduced surface roughness while maintaining high stability in various harsh environments. The optimized PNC films were eventually applied in an X-ray imaging system as scintillators, showing a high spatial resolution above 20 lp/mm. By designing this promising dual organosilicon ligand system for PNC films, our work highlights the crucial influence of the molecular structure of the capping ligands on the optical performance of the PNC film.**

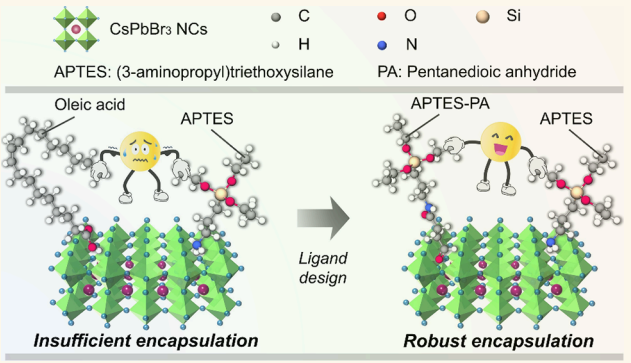

KEYWORDS: *perovskite nanocrystals, ligand design, organosilicon ligands, film formation, reduced scattering, scintillator, X-ray imaging*

1. INTRODUCTION

All-inorganic $CsPbX_3$ (X = Cl, Br, or I) perovskite nanocrystals (PNCs) have attracted tremendous interest owing to their broadly tunable photoluminescence (PL) across 400−700 nm, narrow PL full-width at half-maximum (fwhm), and high PL quantum yield (PLQY).[1−4] Given these appealing features, CsPbX3 NCs demonstrate great potential, especially for applications in optics and photonics, including light-emitting diodes (LEDs),[5−7] displays,[8,9] lasers,[10,11] single-photon source,[12,13] and X-ray scintillators.[14−16] Furthermore, the relatively low formation energy and the high defect tolerance of the lead-halide PNCs enable the preparation of highly fluorescent materials at low temperatures and low cost, hence greatly broadening its application prospects.[17] However, the labile surface and metastable ionic structure of PNCs cause poor stability against heat, moisture, and UV radiation.[18−20] For example, surface decomposition and increased trap state densities of $CsPbX_3$ PNCs are observed under oxygen-rich and humid conditions.[19] The desorption of the surface ligands can destruct the colloidal integrity of PNCs and lead to luminescence quenching.[21]

Aiming at enhancing the stability of PNCs, valuable efforts have been devoted by numerous researchers using the following three strategies: (1) compositional manipulation, such as heterojunction structures (e.g., composite structures of

Received: November 30, 2023
Revised: February 16, 2024
Accepted: February 23, 2024
Published: March 25, 2024

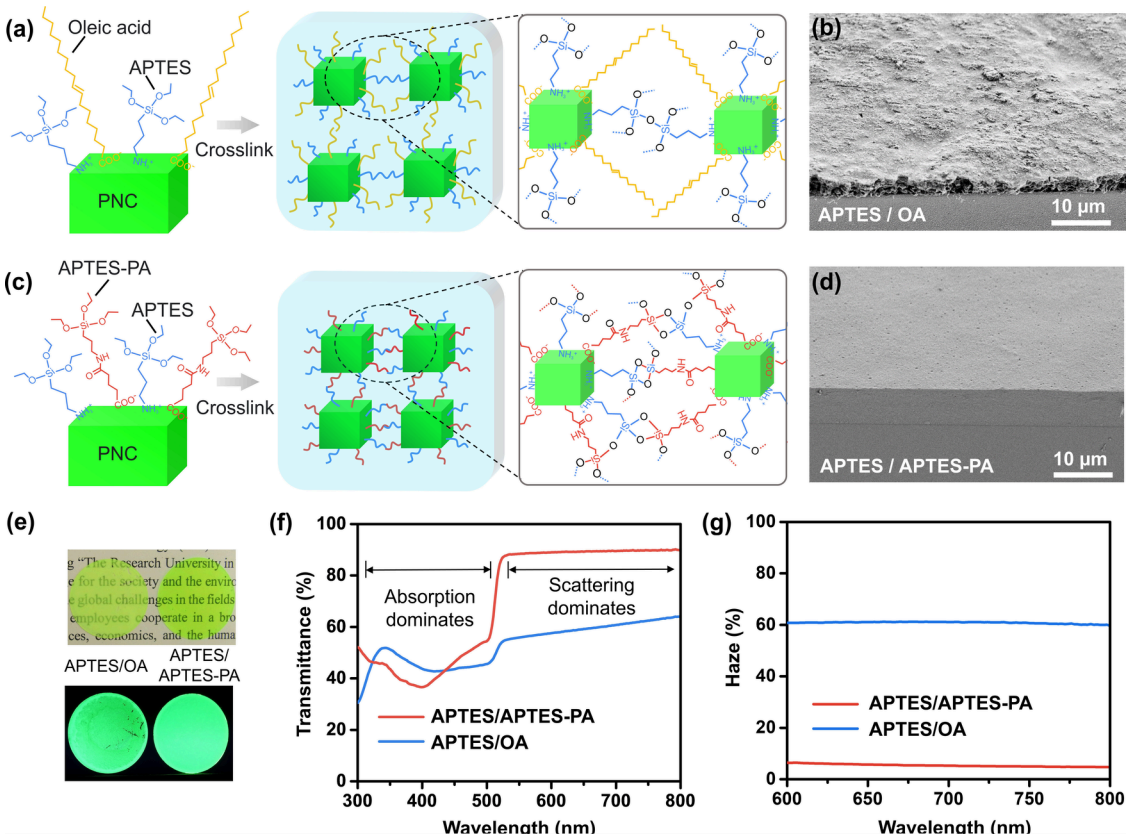

Figure 1. Ligand design for enhancing the compatibility in film-forming systems to improve the film performance. Schematics of the ligand molecules and illustrations of the condensation reactions of (a) conventional APTES/OA ligand system, and (c) proposed APTES/APTES-PA ligand system. Cross-sectional SEM images (with a tilting angle of 45°) of the PNC/silicone films with (b) APTES/OA ligands, and (d) APTES/APTES-PA ligands. e) Photographs of the corresponding PNC/silicone films under white light and UV radiation. (f) Transmittance spectra, and (g) Haze spectra of PNC/silicone films with APTES/APTES-PA ligands and APTES/OA ligands, respectively.

$CsPbBr_3/CsPb_2Br_5$);[22,23] (2) surface modification, such as the introduction of multidentate surface ligands;[24,25] (3) matrix encapsulation, such as embedding PNCs in transparent inorganic oxides or organic polymers (e.g., silicon oxide,[26] alumina,[27] polystyrene (PS),[28] and poly(methyl methacrylate)[29,30]). Among the above strategies, encapsulation based on a solid matrix can provide effective physical isolation of PNC materials from environmental stimuli, including moisture and oxygen, thus significantly improving their stability.

Polymers and inorganic oxides are the most commonly used matrixes for the solid-state encapsulation of PNCs.[31,32] The encapsulation based on inorganic oxides normally enables outstanding stability against heat and UV radiation for PNCs owing to the high bonding energy of the inorganic oxide matrix.[33,34] However, the PNCs encapsulated with an inorganic oxide matrix are prone to exist as insoluble and crumbly solid-like powders, which limits their processability and application prospects.[35,36] In contrast, organic polymer matrix provides excellent solution-processability and film quality for PNCs. Nevertheless, the widely used long carbon chain ligands, including oleic acid (OA) and oleyl amine (OLA), are incompatible with a polymer matrix due to the lack of molecular affinity, resulting in significant aggregations of PNCs and deficient performance of the PNC films.[37,38] In addition, polymer-encapsulated PNCs demonstrate poorer thermal stability and photostability than oxide-encapsulated PNCs, as the polymer matrix itself commonly suffers from aging and yellowing in harsh environments.[39]

In contrast, as an organic−inorganic hybridization, organosilicon-based encapsulation is capable of integrating the advantages of inorganic oxide and organic polymer matrixes, which provides firm protection for PNCs while maintaining good processability for the forming or patterning of PNC films.[40,41] Compared to polymeric encapsulation, the organosilicon matrix enables a firmer connection with the PNCs and superior stability due to the high-density network of the O−Si−O bonds. Compared to inorganic oxide encapsulation, organosilicon molecules can cross-link with each other through condensation reactions, providing competitive processability and compactness for the PNC film. Despite the affecting advantages above, current ligand systems of organosilicon-encapsulated PNCs widely incorporate inert long-chain ligands (e.g., OA), which is necessary to these systems for the synthesis and stabilization of colloidal PNCs.[42] However, the inert long-chain ligands are incompatible with the cross-linking of the organosilicon matrix for film formation.[43,44] In a detailed manner, the long-chain ligands are inert in the condensation reaction of the silicate ligands and their large molecular length potentially suppresses the cross-linking of the organosilicon matrix. Thus, the presence of long-chain ligands ultimately leads to low transparency and a large surface roughness of the PNC film, inhibiting the full potential of the organosilicon-based encapsulation strategy.

To tackle the challenges above, we propose here a double-organosilicon ligand system based on (3-aminopropyl)-triethoxysilane (APTES) and (3-aminopropyl)triethoxysilane

https://doi.org/10.1021/acsnano.3c11991
ACS Nano 2024, 18, 10054−10062

with pentanedioic anhydride (APTES-PA) for fabricating high-performance PNC films. In the system, the inert long-carbon-chain ligands (e.g., OA, OLA) are replaced by the designed APTES-PA ligand to improve the compatibility of the whole colloidal system. The APTES-PA molecule contains multiple silicon-based functional groups that enable its participation in the condensation reactions among silicate bonds to form a well-cross-linked matrix meanwhile contributing to the stabilization of the colloidal PNCs.

With the proposed ligand system, strongly fluorescent PNC/silicone films with high transparency and reduced surface roughness were successfully prepared. Owing to the compact encapsulation of the organosilicon matrix, the obtained PNC films showed decent stability in various harsh environments. The optimized PNC films were eventually applied in an X-ray imaging system as radioluminescence (RL) scintillators, achieving a high spatial resolution above 20 line pairs per millimeter (lp/mm). In our work, we designed a dual-organosilicon ligand system for enhancing the performance of organosilicon-encapsulated PNC films. Moreover, it highlights the important influence of the molecular structure of the surface ligands on the film formation and film performance of PNCs.

2. RESULTS AND DISCUSSION

To enhance the compatibility of the film-forming compounds for organosilicon-encapsulated PNCs, we designed and synthesized a dual-silicone ligand system for the stabilization of PNCs to replace the OA and OLA ligands (Figure 1). The dual-silicone ligand system, which consists of APTES ligands with an amino headgroup and APTES-PA ligands with a carboxyl headgroup, was designed with the inspiration of the classical OA/OLA ligand system. The APTES ligand with an amino headgroup can provide sufficient surface passivation for the PNCs but is unable to provide sufficient colloidal stability for the PNC dispersion.[45,46] The APTES-PA ligand with a longer carbon chain was introduced to impart PNCs to sufficient colloidal stability in weakly polar solvents, as shown in Figure S1 and Figure S2. The designed silicone ligands are attached on the surface of PNCs spontaneously during the synthesis based on ligand-assisted coprecipitation (Figure S3). The function of the APTES-PA ligand as a stabilizer for PNCs is well demonstrated in Figure S4, which proves that it is indispensable in the proposed colloidal systems. After a stable PNC dispersion was obtained, the fine film-forming properties of organosilicon-stabilized colloidal PNCs were demonstrated by a facile solution-casting strategy. The volatilization of solvents and the condensation of the silicate bonds were induced by heating to obtain silicone-encapsulated PNC films (see details in the Experimental Section). The thickness of the PNC film can be altered ranging from submicron scale to micron scale by simply adjusting the concentration of the PNC dispersion and the drop-casting volume (Figure S5). The performance of APTES-PA/APTES-capped PNCs was compared to the conventional APTES/OA ligand group under the same film-forming conditions. In the APTES/OA ligand system, as illustrated in Figure 1a, the long-chain OA ligands cannot participate in the condensation reaction that creates the solid organosilicon matrix and contributes only to the surface passivation of PNCs. Moreover, due to the large length of the ligands, the presence of the long-chain OA molecules suppresses the contact and cross-linking among APTES ligands during condensation, resulting in rough surface morphology and poor compactness of the PNC/silicone film (Figure 1b and Figure S6). As exhibited in Figure 1c, the designed APTES-PA molecule is shorter than the OA molecule and contains multiple silicone functional groups. In the condensation process, the ethoxy-silane-ether groups of APTES and APTES-PA ligands are triggered by trace moisture in the solvent or ambient air and then creating massive cross-linking Si−O−Si bonds which form the solid matrix for the $CsPbBr_3$ NCs.[47,48] The dense cross-linking joints enable superior film quality (Figure 1d). In addition, compared to the OA ligand, owing to the reduced molecule size and higher cross-linking efficiency of the APTES-PA ligand, a relatively lower quantity of the capping ligands is demanded to provide sufficient encapsulation, which potentially elevates the maximum PNC loading in the film. Compared to the OA-capped PNC film, the enhanced transparency and reduced scattering of the APTES-PA-capped PNC film are visually demonstrated in Figure 1e. By replacing the OA ligand with the APTES-PA ligand, the transmittance of the silicone-encapsulated PNC film is significantly improved and its overall haze value greatly diminishes in the nonabsorbing region (Figure 1e, f). Here, PNC films with a thickness of around 5 μm were deposited on glass substrates for the measurement. The deficient transmittance of the APTES/OA sample is attributed to the rough surface and microscale protrusions of the film, which generate massive light scattering and reflection. The APTES-PA encapsulation method based on the condensation of the surface ligands can effectively avoid the aggregation problem of PNCs caused by the introduction of exogenous packaging matrix (e.g., polystyrene), as shown in Figure S7. In addition, with good affinity of the capping ligands and compact encapsulation, the fabrication of flexible PNC/silicone thin films is possible. An example of coating a PNC/silicone film on a polyethylene terephthalate foil is shown in Figure S8. The flexible PNC/silicone film exhibits strong fluorescence under UV radiation in a curved state. In all, compared with the conventional APTES/OA ligand system, the proposed APTES/APTES-PA ligand system significantly improves the quality of the PNC/silicone film for better compactness, higher transmittance, and reduced scattering. These enhanced optical performances are critical for lasing,[49,50] X-ray imaging,[51] and other applications where good packaging and optical quality are needed. A characterization of the amplification of spontaneous emission (ASE) of the PNC/silicone film was conducted, and the PL spectra are shown in Figure S9. With the pumping of a femtosecond laser (peak wavelength: 342 nm), the PNC/silicone film obtained an ASE threshold of between 17.1−34.2 $\mu J/cm^2$. The proposed high-performance PNC/silicone film with high transparency and outstanding stability is thus promising for a wide range of optical applications.

Fourier transform infrared (FTIR) measurements were conducted to characterize the chemical bonds of the PNC composite films. As shown in Figure 2a, the FTIR spectra reveal a dramatic increase of the Si−O−Si and Si−O−C bonds for APTES/OA and APTES/APTES-PA samples compared to the OLA/OA ligand group, verifying the occurrence of the hydrolysis and the practical wrapping of the silicon matrix for PNCs. Besides, the APTES/APTES-PA sample shows an obvious weakening of the characteristic peak of the C−H bond due to the absence of OA ligands. The results of X-ray diffraction (XRD) indicate that both APTES/APTES-PA and APTES/OA encapsulated PNCs have only the $CsPbBr_3$ phase

https://doi.org/10.1021/acsnano.3c11991
ACS Nano 2024, 18, 10054−10062

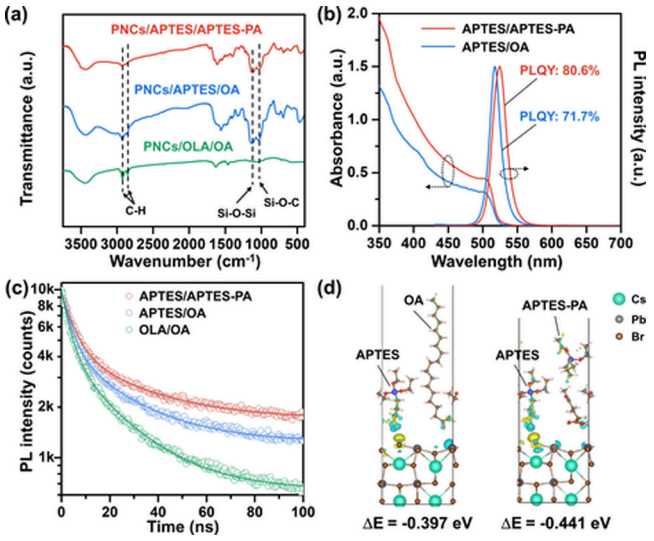

Figure 2. Surface chemistry of designed silicone ligands. (a) FTIR spectra, and (b) absorbance and emission spectra of the PNC composite films with different ligands. (c) Time-resolved PL decay curves and the corresponding biexponential fitting curves of the PNC films. (d) Results of the DFT calculations of the charge density redistribution of the optimized $CsPbBr_3$-001 surfaces capped with APTES/OA and APTES/APTES-PA ligand groups, respectively.

without other nonluminescent phases (Figure S10). The as-prepared PNCs exhibit a cubic structure with a particle size of ~11 nm, as shown in the TEM images (Figure S11). The dense and well-separated PNCs homogeneously distribute in the organosilicon matrix network without agglomeration. The absorbance spectra of the composite films have the typical shape of $CsPbBr_3$ NCs. The emission peak of the PNC/APTES/APTES-PA film is centered at 526 nm with a fwhm of 23 nm. The PLQY of the sample is measured to amount to 80.6% with a high PNC concentration of around 36 wt % based on the 3 M measurement procedure (Figure S12).[52] By reducing the film thickness, the PLQY of the PNC/APTES/APTES-PA sample can be further improved (Figure S5). This can be attributed to a diminished influence of reabsorption and thus more complete outcoupling. The APTES/OA sample shows a lower PLQY of 71.7% with the same PNC loading but obtains a smaller fwhm of 20 nm. The high PLQY of the PNC/APTES/APTES-PA sample indicates the robust surface trap passivation and improved dispersibility brought by the APTES/APTES-PA ligands, while the slightly broadened emission peak can be attributed to the enhanced hydrolysis capability and efficiency. As illustrated in Figure S13, the dual-organosilicon ligand system could generate a small number of undesired silica nanospheres during the synthesis of PNCs. The spatial confinement effect of the silica nanospheres to the precursor solution and crystal growth would lead to the size inhomogeneities of PNCs, resulting in a broadening of the emission peak of PNC film. The time-resolved PL decays are measured to explore the carrier dynamics in the NCs (Figure 2c). The corresponding biexponential fitting curves are exhibited as well and are applied for the calculation of the average PL lifetime. In detail, the fitted intensity average PL lifetimes of the APTES/APTES-PA sample, the APTES/OA sample, and the OLA/OA sample are 22.7, 20.0, and 17.7 ns, respectively. Combined with the PLQY values, the radiative recombination rate (K_r) and the nonradiative recombination rate (K_{nr}) of the films are calculated and shown in Table S1. The longer average PL lifetime and lower K_{nr} of the APTES/APTES-PA sample, along with the high PLQY, suggest an effective surface defect passivation of the organosilicon coating with the proposed ligands.[53] Here, the passivation effect of the APTES/APTES-PA ligands on the PNCs is exhibited in two aspects. First, the ligand capping on the surface of PNCs in the solvent environment efficiently passivates the unsaturated dangling bonds on the surface of the PNCs. Second, the cross-linking of the ligands forms a dense O−Si−O barrier around the PNCs, generating effective protection for the PNCs toward environmental stimuli.[35] The strength of the passivation effect of the surface ligand on the surface defects of the PNCs may be implied by the binding energy of the ligand to the surface of PNCs.[46,54] The binding energies between the ligands and the PNC surface were calculated by employing density functional theory (DFT) methods. The models of the calculated molecules and crystal surface are shown in Figure S14. The charge density redistributions of the $PbBr_2$-rich surfaces (001) of the $CsPbBr_3$ crystal attached with APTES/OA ligands and APTES/APTES-PA ligands are shown in Figure 2d. In both cases, the APTES ligands attach on the Pb atoms with similar charge redistributions, where the electron accumulation (yellow cloud) is localized on the ammonium group and the electron dilution (cyan cloud) is evident along the surface Pb atoms. Moreover, the APTES-PA ligand shows a larger electron dilution cloud than the OA ligand on the PNC surface. As a result, the ligand combination of APTES/APTES-PA obtains an overall binding energy of −0.441 eV, which is higher than that of the APTES/OA ligand group (−0.397 eV) in absolute values. The strong binding of the proposed APTES-PA ligand on the PNC surface indicates better surface passivation.[25]

In silicone-encapsulated PNC systems, the strong O−Si−O bond provides better protection for PNCs against environmental factors relative to widely used PS-encapsulated systems. Figure 3 shows the normalized PL intensity of the PNC/APTES/APTES-PA films after heating to elevated temperatures, exposure to UV radiation, water immersion, and solvent immersion, respectively. $CsPbBr_3$ PNC film packaged by PS polymer and PNC/APTES/OA sample were incorporated in the test as a reference. The PNC concentration of the PNC films here was 36 wt % (see details in the Experimental Section). As shown in Figure 3a, the PNC/APTES/APTES-PA sample exhibits higher remaining PL intensity than the PNC/APTES/OA and PNC/PS samples after being heated to different temperatures. Specifically, the PNC/APTES/APTES-PA film maintains 62.3% of the PL intensity after the thermal treatment up to 180 °C, while only 36.8% of PL intensity is maintained for PNC/PS film and 55.2% for PNC/APTES/OA sample. The improved thermal stability of the PNC/APTES/APTES-PA film can be attributed to the decent protection from the organosilicon matrix that passivates the surface defects and suppresses the phase transition of PNCs at high temperature.[55] Moreover, the thermal performance of the matrix itself would affect the stability of PNC films as well.[56] As the glass transition temperature of the PS matrix is relatively low, morphology defects (such as air bubbles) are generated inside the PNC/PS film when the temperature is above 110 °C, resulting in a serious impairment to the film quality. On the contrary, organosilicon-based encapsulation can prevent morphology defects and deformation for this condition. Figure 3b shows the temporal evolution of the PL intensities of the

https://doi.org/10.1021/acsnano.3c11991
ACS Nano 2024, 18, 10054−10062

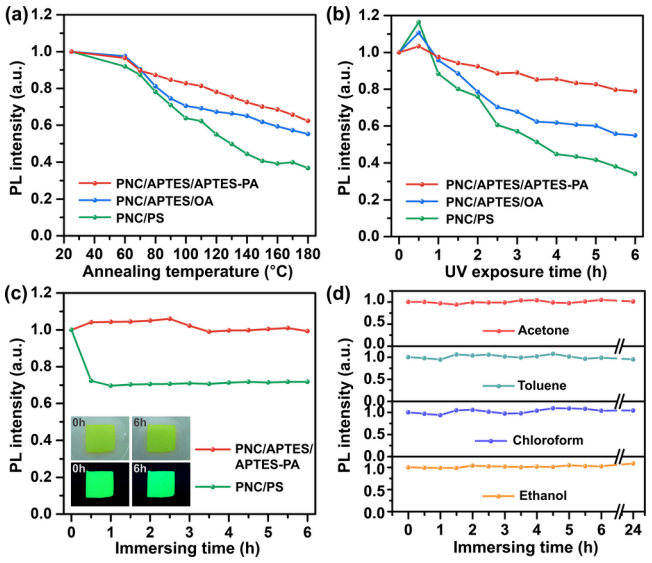

Figure 3. Stability of the PNC/silicone films. (a) Normalized PL intensities of PNC/APTES/APTES-PA, PNC/APTES/OA, and PNC/PS films after heating to different temperatures. The heating process lasted 10 min at each temperature. For each data point, the sample was cooled down to room temperature. (b) PL intensities of PNC films under UV irradiation (365 nm) with the power of 1.5 mW/cm^2. (c) PL intensity for different immersion times in water at 22 °C. The PNC films were directly immersed in deionized water. The insets are the photographs of the PNC/APTES/APTES-PA sample after 0 and 6 h of water immersion under white light (upper row) and 365 nm UV excitation (bottom row), respectively. (d) Solvent resistance of PNC/APTES/APTES-PA film by immersing the film in acetone, toluene, chloroform, and ethanol, respectively.

three types of PNC film under strong UV radiation (Proma 140007 UV exposer) of 1.5 mW/cm^2. The PNC/APTES/APTES-PA sample reveals better photostability with a remaining PL intensity of 78.9% after 6 h of UV radiation, while the PL intensity of the PNC/PS sample reduces to 34.1% and the PL intensity of the PNC/APTES/OA diminishes to 55.0%. It indicates that the compact encapsulation of the silicone coating effectively inhibits the photodegradation of PNCs.[55] To evaluate the water resistance, a water immersion test was conducted for the PNC films. During this test, the sample films were taken out of water and dried at 22 °C for the PL measurement. Since the PNC/APTES/OA sample is crumbly and is not attaching to the substrate firmly, part of the PNC would be removed during the immersion test, which impairs the accuracy of the measurement. Thus, it is not included in the immersion tests. As illustrated in Figure 3c, the fluorescence of the PNC/APTES/APTES-PA film is steady during 6 h of the water immersion with a maintaining PL intensity of 99.3%, while the retained PL intensity of the PNC/PS film is 71.7%. The PL reduction of the PNC/PS film can be attributed to the incomplete encapsulation of the PS polymer due to the high PNC loading. Figure 3d shows the high resistance of the PNC/APTES/APTES-PA film to organic solvents including acetone, toluene, chloroform, and ethanol. In all the solvents above, the PNC/APTES/APTES-PA films hardly show a reduction in PL intensity after 24 h of solvent immersion, indicating the good protection of NCs by the organosilicon matrix. The excellent resistance to the organic solvents enables, e.g., a better potential for further patterning processes that incorporate organic solvents. The comprehensive stability tests reveal the high robustness of the PNC/silicone film with the designed ligand system and the great potential to be practically applied in optical systems. Besides, a detailed summary of the PLQY and stability performance of PNC/organosilicon compounds from relevant literature was listed for comparison and analysis (Table S2).

To evaluate the performance of the proposed PNC/APTES/APTES-PA film for X-ray scintillation and imaging applications, a series of tests were conducted using a microfocus X-ray tube (XT9160-DED, Viscom) as the radiation source. Here, we will refer to the PNC/APTES/APTES-PA sample as a PNC/Silicone film in the following. The thickness of the PNC/silicone film used here was approximately 25 μm. The RL spectra of the PNC/silicone film and a commonly used lutetium−yttrium oxyorthosilicate (LYSO) scintillator are shown in Figure 4a. The PNC/silicone film exhibits a narrow emission peak with a fwhm of 21 nm, while the LYSO film shows a much broader RL peak. The narrow emission peak is advantageous for achieving the best read-out efficiency by matching the emission peak with the response peak of photodetectors, including photomultiplier tubes, photodiodes, and CCD or CMOS cameras.[57,58] The integrated RL intensity of the PNC/silicone film as a function of the dose rate of X-ray excitation is shown in Figure 4b. A linear fitting line is calculated based on the measured data points, and a high linearity is shown with a coefficient of determination of 0.993. The linear response of the PNC/silicone film enables its practical application for X-ray detection. Herein, a custom X-ray imaging system was built according to the scheme illustrated in Figure 4c. The photograph and details of the imaging system are shown in Figure S15. Based on this system, the X-ray imaging test was conducted with a standard X-ray line-pair test pattern (PTW L659035) for characterizing the spatial resolution of the PNC scintillator. The imaging test with the line-pair test pattern as the detected sample was conducted with a tube voltage of 60 kV and a dose rate of 6.58 mGy/s, while the imaging tests with microelectronic chip and ball-point pen as the detected samples were conducted with a tube voltage of 30 kV and a dose rate of 3.84 mGy/s. All the X-ray images in this figure were darkfield-corrected. Figure 4d shows the X-ray image of the pattern chart with a 4× objective. Owing to the reduced light scattering and the low thickness of the PNC/silicone film, the line pairs at the positions with a spatial resolution of up to 20 lp/mm can be clearly distinguished. As displayed in Figure 4e, an enlarged view of the bottom part of the line pattern was acquired by using a 10× objective lens. More details of the line pattern are presented, and the gaps between the lines can be easily distinguished. The white flash dots in the image are caused by X-ray photons directly impinging on the CMOS camera. By extracting the gray values across the line pattern from the X-ray image, gray value profiles of the line pairs with different spatial resolutions are obtained and depicted in Figure 4f. The X-ray images of the line pair pattern of 6 and 10 lp/mm can be found in Figure S16. Clear peaks and valleys of the profile curves can be observed up to the highest measured spatial resolution. With smaller gaps between the lines, the gray value contrast gradually reduces. Yet, the results indicate that the 25 μm thick PNC/silicone film in combination with the presented imaging system can achieve a spatial resolution of at least 20 lp/mm with a contrast of >0.2. For comparison, we summarize the encapsulating matrix types and other parameters of the

https://doi.org/10.1021/acsnano.3c11991
ACS Nano 2024, 18, 10054−10062

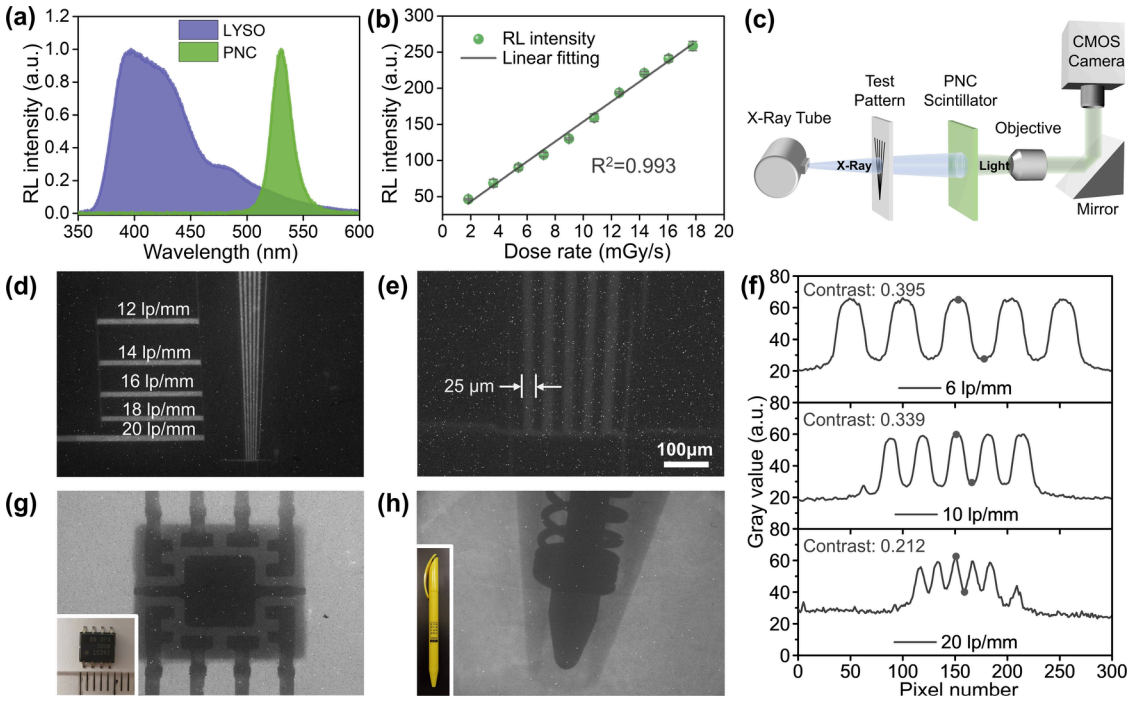

Figure 4. X-ray scintillation and imaging demonstrations. (a) Normalized RL spectra of a PNC/silicone film and a lutetium−yttrium oxyorthosilicate (LYSO) film under X-ray excitation. (b) Integrated radioluminescence (RL) intensity of a PNC/silicone film in dependence on the X-ray dose rate. The behavior can be well-fitted with a linear function. (c) The schematic of the X-ray imaging system with PNC scintillator. (d) X-ray images of a resolution test pattern using PNC/silicone film (tube voltage: 60 kV, dose rate: 6.58 mGy/s) with a 4× objective lens and (e) a 10× objective lens. (f) Gray-value profiles of the line patterns extracted from the corresponding positions in the X-ray images in (e) and Figure S16, as well as the corresponding contrast values. X-ray images of (g) a microelectronic chip, and (h) a ball-point pen (tube voltage: 30 kV, dose rate: 3.84 mGy/s). The inserts are photos of the respective samples.

previously reported $CsPbBr_3$ PNC scintillators in Table S3, which indicates that the proposed PNC/silicone film in this work is competitive with other PNC scintillators in terms of high spatial resolution. An even better resolution could be achievable with a more advanced optical microscope system. As shown in Figure 4f and Figure 4e, X-ray images of an amplifier chip (OPA 300A, Burr-Brown) and a ball-point pen are obtained using the PNC/silicone scintillator as demos. Clear contrasts are generated in both images to distinguish the plastic cover and the metal part in detail. For the electronic package, the thin metal wires (with a thickness of around 50 μm) inside the component can be clearly observed in the image, indicating the good resolution of the scintillator film. To demonstrate the imaging performance of the PNC scintillator on biological samples, we have included an X-ray image of a chicken foot with an inserted syringe needle, as shown in Figure S17. The different biological tissues, the bone, and the metallic syringe needle are clearly visible. Moreover, a high dose rate stability test was conducted on the PNC/silicone scintillator by exposing the sample to continuous X-ray radiation (60 kV/24.7 mGy/s). As illustrated in Figure S18, the PNC/silicone sample retains 74.7% of the RL intensity after 180 min of X-ray exposure, indicating decent stability under X-ray exposure.

3. CONCLUSION

In summary, we presented a full organosilicon-based ligand system for the encapsulation of PNCs and successfully prepared a high-performance fluorescent PNC/silicone film. The compactness of the encapsulating matrix was effectively improved by the sufficient cross-links of the proposed ligand system, resulting in enhanced transparency and stability of the PNC film while maintaining high PLQY. Besides, due to the firm encapsulation and decent passivation of the proposed capping ligands, the PNC/silicone film showed superior stability compared to the PS-encapsulated PNC film under the harsh conditions of high temperature and intense UV radiation. Good resistance toward the water and organic solvents was revealed, as well. The PNC/silicone films were applied as scintillators for X-ray imaging. By incorporation of the PNC/silicone film, the imaging system obtained a high resolution of more than 20 lp/mm with good contrast. Overall, the proposed ligand system for PNCs enables low-cost fabrication of high-performance PNC films and is compatible with various depositing and patterning techniques. Based on this work, our next step is dedicated to extending this strategy to other types of lead halide PNCs for achieving full-color fluorescence.

4. EXPERIMENTAL SECTION

Synthesis of APTES-PA Ligands. GA (0.6 g, 5 mmol) was dissolved in THF (10 mL), and APTES (1.35 g, 5 mmol) was added slowly in succession at 65 °C under stirring. After reacting for 12 h, the red crude product was extracted by using a rotary evaporator and directly used without further purification. A small part of the obtained sample was dissolved in deuterated DMSO solvent for measuring its hydrogen-1 nuclear magnetic resonance spectrum.

Synthesis of PNC Dispersion. In a typical synthesis of APTES-PA capped PNCs, the 0.2 mmol of $PbBr_2$ and 0.2 mmol of CsBr were mixed in 5 mL of DMF with stirring until totally dissolved. After that, 120 μL of APTES and 110 μL of compound APTES-PA were added into precursors. After 5 min of stirring until clarification, 500 μL of the precursor solution was added into 10 mL of the solvent mixture of

https://doi.org/10.1021/acsnano.3c11991
ACS Nano 2024, 18, 10054−10062

DCM and toluene (volume ratio of 1:1) with vigorous stirring. A clear and bright green PNC colloidal dispersion was obtained for subsequent film formation. The colloidal dispersion was drop-cast onto clean glass slides and then dried in a vacuum oven at 65 °C to form a solid film. The film thickness was adjusted by the casting volume and the amount of the casting cycle. The calculated concentration of the PNCs in the solid film is about 36 wt %. For the synthesis of PNCs capped with APTES and OA ligands, the APTES-PA ligand was replaced by OA ligand with the same amount.

Preparation of PNC/PS Films. Oleic-acid-capped PNC dispersion in toluene solvent with a concentration of 10 mg/mL was first prepared. Subsequently, 128 mg of PS (Sigma-Aldrich, 96 000 Da) powder were added into 7.2 mL of the PNC dispersion followed by 4 h of magnetic stirring to completely dissolve the PS polymer and obtain a homogeneous mixture. Consequently, the solution mixture was drop-cast on clean glass substrates with a volume of 180 μL and dried at room temperature. PNC/PS films were obtained after total evaporation of the toluene solvent.

Stability Tests. The PL measurements in the stability characterization were conducted in an integrating sphere in the glovebox and excited by a UV-LED chip (NCSU276A, Nichia) driven by a precise power supply (Source Meter 2450, Keithley) with a current of 20 mA. For the thermal stability test, the sample films were heated on a hot plate at different temperatures for 10 min in the glovebox for each heating round and measured after their cooling down to room temperature. The UV aging test was conducted with a UV exposure box (Proma 140007) with a power of 1.5 mW/cm^2 in the atmosphere. The resistance tests against water and organic solvents were tested by directly immersing the sample films into the corresponding liquid in the atmosphere and drying by a nitrogen gun before the PL measurement.

X-ray Scintillation and Imaging Tests. The RL and imaging measurements were conducted using an X-ray tube (XT9160-DED, Viscom) with a tungsten target and aluminum filtration (0.4 mm) in a dark room. For the RL and linearity measurements, a 3D-printing holder for the sample films and a UV−vis spectrometer (USB200+, Ocean Optics) were utilized. During the measurement, the tube voltage was fixed to 30 kV and the tube current was varied from 0.2 to 2.4 mA. The exact dose rate of the excitation was valued by a dosimeter (MagicMaX, IBA) equipped with an RQA detector (IBA). A monochrome CMOS camera (DMK21BZU04, Imaging Source) with a pixel size of 5.6 μm × 5.6 μm, objective lens (Newport Corporation), and test pattern (PTW L659035) were used for the imaging. The exposure time of the X-ray images in the imaging test was 5 s. The contrast of the gray value image was calculated as the following equation: Contrast = $(I_{max} - I_{min})/(I_{max} + I_{min})$; where the maximal and minimal intensity were marked on the line profiles as dots.

ASSOCIATED CONTENT

Supporting Information

The Supporting Information is available free of charge at https://pubs.acs.org/doi/10.1021/acsnano.3c11991.

Additional details regarding materials and characterizations, chemical equation of the synthesis of APTES-PA ligand, Hydrogen-1 nuclear magnetic resonance spectrum of the APTES-PA compound, illustration of the synthesis and film formation process, photographs and illustrations of capping ligands of the PNC toluene dispersions, photographs and PLQYs of PNC films with different thickness, atomic force microscopy images of the PNC/silicone films, microscope images of PNC films, photographs of the flexible PNC/silicone film, illustration and PL spectra of the amplification of spontaneous emission of PNC/silicone film, X-ray diffraction patterns of PNC films, transmission electron microscopy image of PNC film, PL spectra of PNC films for PLQY calculation, schematic of the synthesis of PNCs, details of the fitting of PL decays, models of the ligand molecules for DFT calculation, comparative summary about the stabilities of organosilicon-encapsulated PNCs, photograph of the X-ray imaging system, X-ray images of line pair patterns, photograph and X-ray imaging demo of a biological sample, comparative summary about the spatial resolution of X-ray imaging with PNC scintillator, lifetime of PNC/APTES/APTES-PA film under X-ray radiation (PDF)

AUTHOR INFORMATION

Corresponding Authors

Guocan Jiang − *Zhejiang Institute of Photoelectronics, Department of Physics, Zhejiang Normal University, Jinhua 321004 Zhejiang, P. R. China; Physical Chemistry, Technische Universität Dresden (TUD), 01069 Dresden, Germany;* orcid.org/0009-0005-5565-6052; Email: gcjiang@zjnu.edu.cn

Uli Lemmer − *Light Technology Institute, Karlsruhe Institute of Technology (KIT), 76131 Karlsruhe, Germany;* orcid.org/0000-0001-9892-329X; Email: uli.lemmer@kit.edu

Authors

Junchi Chen − *Light Technology Institute, Karlsruhe Institute of Technology (KIT), 76131 Karlsruhe, Germany;* orcid.org/0000-0002-2582-4642

Elias Hamann − *Institute for Photon Science and Synchrotron Radiation, Karlsruhe Institute of Technology (KIT), 76344 Eggenstein Leopoldshafen, Germany;* orcid.org/0000-0002-0623-9069

Henning Mescher − *Light Technology Institute, Karlsruhe Institute of Technology (KIT), 76131 Karlsruhe, Germany;* orcid.org/0000-0001-7083-6063

Qihao Jin − *Light Technology Institute, Karlsruhe Institute of Technology (KIT), 76131 Karlsruhe, Germany;* orcid.org/0000-0002-1546-7637

Isabel Allegro − *Light Technology Institute, Karlsruhe Institute of Technology (KIT), 76131 Karlsruhe, Germany;* orcid.org/0000-0001-9663-4910

Philipp Brenner − *ZEISS Innovation Hub @ KIT, 76344 Eggenstein-Leopoldshafen, Germany*

Zhengquan Li − *Zhejiang Institute of Photoelectronics, Department of Physics, Zhejiang Normal University, Jinhua 321004 Zhejiang, P. R. China;* orcid.org/0000-0002-0084-5113

[#]Nikolai Gaponik − *Physical Chemistry, Technische Universität Dresden (TUD), 01069 Dresden, Germany;* orcid.org/0000-0002-8827-2881

Alexander Eychmüller − *Physical Chemistry, Technische Universität Dresden (TUD), 01069 Dresden, Germany;* orcid.org/0000-0001-9926-6279

Complete contact information is available at: https://pubs.acs.org/10.1021/acsnano.3c11991

Notes

The authors declare no competing financial interest.

[#]Deceased June 1, 2023.

https://doi.org/10.1021/acsnano.3c11991
ACS Nano 2024, 18, 10054−10062

ACKNOWLEDGMENTS

We dedicate this work to our beloved Prof. Nikolai Gaponik. The authors gratefully acknowledge support from the Karlsruhe School of Optics & Photonics, the China Scholarship Council (No. 201906150139), the National Natural Science Foundation of China (21975223), and Natural Science Foundation of Zhejiang Province (LZ22B030002). This research has also been funded by the Deutsche Forschungsgemeinschaft (DFG, German Research Foundation) under Germany's Excellence Strategy via the Excellence Cluster 3D Matter Made to Order (EXC-2082/1-390761711), the DFG research training group project (DFG RTG 2767, Supracolloidal Structures), and the DFG priority program (SPP 1839, Tailored Disorder).

REFERENCES

(1) Protesescu, L.; Yakunin, S.; Bodnarchuk, M. I.; Krieg, F.; Caputo, R.; Hendon, C. H.; Yang, R. X.; Walsh, A.; Kovalenko, M. V. Nanocrystals of Cesium Lead Halide Perovskites ($CsPbX_3$, X = Cl, Br, and I): Novel Optoelectronic Materials Showing Bright Emission with Wide Color Gamut. *Nano Lett.* **2015**, *15*, 3692−3696.

(2) Akkerman, Q. A.; Abdelhady, A. L.; Manna, L. Zero-Dimensional Cesium Lead Halides: History, Properties, and Challenges. *J. Phys. Chem. Lett.* **2018**, *9*, 2326−2337.

(3) Huang, C.-Y.; Li, H.; Wu, Y.; Lin, C.-H.; Guan, X.; Hu, L.; Kim, J.; Zhu, X.; Zeng, H.; Wu, T. Inorganic Halide Perovskite Quantum Dots: A Versatile Nanomaterial Platform for Electronic Applications. *Nano-Micro Lett.* **2023**, *15*, 16.

(4) Chang, S.; Bai, Z.; Zhong, H. In Situ Fabricated Perovskite Nanocrystals: A Revolution in Optical Materials. *Adv. Opt. Mater.* **2018**, *6*, No. 1800380.

(5) Wan, Q.; Zheng, W.; Zou, C.; Carulli, F.; Zhang, C.; Song, H.; Liu, M.; Zhang, Q.; Lin, L. Y.; Kong, L.; Li, L.; Brovelli, S. Ultrathin Light-Emitting Diodes with External Efficiency over 26% Based on Resurfaced Perovskite Nanocrystals. *ACS Energy Lett.* **2023**, *8*, 927−934.

(6) Chen, J.; Zhao, Q.; Yu, B.; Lemmer, U. A Review on Quantum Dot-Based Color Conversion Layers for Mini/Micro-LED Displays: Packaging, Light Management, and Pixelation. *Adv. Opt. Mater.* **2024**, *12*, No. 2300873.

(7) Zhao, B.; Vasilopoulou, M.; Fakharuddin, A.; Gao, F.; Mohd Yusoff, Abd. R. B.; Friend, R. H.; Di, D. Light Management for Perovskite Light-Emitting Diodes. *Nat. Nanotechnol.* **2023**, *18*, 981−992.

(8) Liao, S.; Yang, Z.; Lin, J.; Wang, S.; Zhu, J.; Chen, S.; Huang, F.; Zheng, Y.; Chen, D. A Hierarchical Structure Perovskite Quantum Dots Film for Laser-Driven Projection Display. *Adv. Funct. Mater.* **2023**, *33*, No. 2210558.

(9) Hu, H.; Levchuk, I.; Kalkowski, F.; Elia, J.; Osvet, A.; Brabec, C. J. Engineering Stable Perovskite Quantum Dot Films for High Color Purity Display Applications. *ACS Energy Lett.* **2023**, *8*, 4380−4385.

(10) Zhang, H.; Wen, W.; Du, B.; Zhou, L.; Chen, Y.; Feng, S.; Zou, C.; Wu, L.; Fan, H. J.; Gao, W.; Sun, H.; Shang, J.; Yu, T. Stable Continuous-Wave Lasing from Discrete Cesium Lead Bromide Quantum Dots Embedded in a Microcavity. *Nanoscale Horiz.* **2023**, *8*, 1403−1410.

(11) Chen, J.; Du, W.; Shi, J.; Li, M.; Wang, Y.; Zhang, Q.; Liu, X. Perovskite Quantum Dot Lasers. *InfoMat* **2020**, *2*, 170−183.

(12) Zhu, C.; Marczak, M.; Feld, L.; Boehme, S. C.; Bernasconi, C.; Moskalenko, A.; Cherniukh, I.; Dirin, D.; Bodnarchuk, M. I.; Kovalenko, M. V.; Rainò, G. Room-Temperature, Highly Pure Single-Photon Sources from All-Inorganic Lead Halide Perovskite Quantum Dots. *Nano Lett.* **2022**, *22*, 3751−3760.

(13) Rainò, G.; Landuyt, A.; Krieg, F.; Bernasconi, C.; Ochsenbein, S. T.; Dirin, D. N.; Bodnarchuk, M. I.; Kovalenko, M. V. Underestimated Effect of a Polymer Matrix on the Light Emission of Single $CsPbBr_3$ Nanocrystals. *Nano Lett.* **2019**, *19*, 3648−3653.

(14) Chen, Q.; Wu, J.; Ou, X.; Huang, B.; Almutlaq, J.; Zhumekenov, A. A.; Guan, X.; Han, S.; Liang, L.; Yi, Z.; Li, J.; Xie, X.; Wang, Y.; Li, Y.; Fan, D.; Teh, D. B. L.; All, A. H.; Mohammed, O. F.; Bakr, O. M.; Wu, T.; Bettinelli, M.; Yang, H.; Huang, W.; Liu, X. All-Inorganic Perovskite Nanocrystal Scintillators. *Nature* **2018**, *561*, 88−93.

(15) Heo, J. H.; Shin, D. H.; Park, J. K.; Kim, D. H.; Lee, S. J.; Im, S. H. High-Performance Next-Generation Perovskite Nanocrystal Scintillator for Nondestructive X-Ray Imaging. *Adv. Mater.* **2018**, *30*, No. 1801743.

(16) Zhou, Y.; Chen, J.; Bakr, O. M.; Mohammed, O. F. Metal Halide Perovskites for X-Ray Imaging Scintillators and Detectors. *ACS Energy Lett.* **2021**, *6*, 739−768.

(17) Shamsi, J.; Urban, A. S.; Imran, M.; De Trizio, L.; Manna, L. Metal Halide Perovskite Nanocrystals: Synthesis, Post-Synthesis Modifications, and Their Optical Properties. *Chem. Rev.* **2019**, *119*, 3296−3348.

(18) Liu, M.; Wan, Q.; Wang, H.; Carulli, F.; Sun, X.; Zheng, W.; Kong, L.; Zhang, Q.; Zhang, C.; Zhang, Q.; Brovelli, S.; Li, L. Suppression of Temperature Quenching in Perovskite Nanocrystals for Efficient and Thermally Stable Light-Emitting Diodes. *Nat. Photonics* **2021**, *15*, 379−385.

(19) Huang, S.; Li, Z.; Wang, B.; Zhu, N.; Zhang, C.; Kong, L.; Zhang, Q.; Shan, A.; Li, L. Morphology Evolution and Degradation of $CsPbBr_3$ Nanocrystals under Blue Light-Emitting Diode Illumination. *ACS Appl. Mater. Interfaces* **2017**, *9*, 7249−7258.

(20) Huang, H.; Bodnarchuk, M. I.; Kershaw, S. V.; Kovalenko, M. V.; Rogach, A. L. Lead Halide Perovskite Nanocrystals in the Research Spotlight: Stability and Defect Tolerance. *ACS Energy Lett.* **2017**, *2*, 2071−2083.

(21) De Roo, J.; Ibáñez, M.; Geiregat, P.; Nedelcu, G.; Walravens, W.; Maes, J.; Martins, J. C.; Van Driessche, I.; Kovalenko, M. V.; Hens, Z. Highly Dynamic Ligand Binding and Light Absorption Coefficient of Cesium Lead Bromide Perovskite Nanocrystals. *ACS Nano* **2016**, *10*, 2071−2081.

(22) Zhang, X.; Xu, B.; Zhang, J.; Gao, Y.; Zheng, Y.; Wang, K.; Sun, X. W. All-Inorganic Perovskite Nanocrystals for High-Efficiency Light Emitting Diodes: Dual-Phase $CsPbBr_3$ -$CsPb_2Br_5$ Composites. *Adv. Funct. Mater.* **2016**, *26*, 4595−4600.

(23) Jia, C.; Li, H.; Meng, X.; Li, H. $CsPbX_3$ /Cs_4 PbX_6 Core/Shell Perovskite Nanocrystals. *Chem. Commun.* **2018**, *54*, 6300−6303.

(24) Wang, S.; Du, L.; Jin, Z.; Xin, Y.; Mattoussi, H. Enhanced Stabilization and Easy Phase Transfer of $CsPbBr_3$ Perovskite Quantum Dots Promoted by High-Affinity Polyzwitterionic Ligands. *J. Am. Chem. Soc.* **2020**, *142*, 12669−12680.

(25) Pan, J.; Shang, Y.; Yin, J.; De Bastiani, M.; Peng, W.; Dursun, I.; Sinatra, L.; El-Zohry, A. M.; Hedhili, M. N.; Emwas, A.-H.; Mohammed, O. F.; Ning, Z.; Bakr, O. M. Bidentate Ligand-Passivated $CsPbI_3$ Perovskite Nanocrystals for Stable Near-Unity Photoluminescence Quantum Yield and Efficient Red Light-Emitting Diodes. *J. Am. Chem. Soc.* **2018**, *140*, 562−565.

(26) An, M. N.; Park, S.; Brescia, R.; Lutfullin, M.; Sinatra, L.; Bakr, O. M.; De Trizio, L.; Manna, L. Low-Temperature Molten Salts Synthesis: $CsPbBr_3$ Nanocrystals with High Photoluminescence Emission Buried in Mesoporous SiO_2. *ACS Energy Lett.* **2021**, *6* (3), 900−907.

(27) Li, Z.; Kong, L.; Huang, S.; Li, L. Highly Luminescent and Ultrastable $CsPbBr_3$ Perovskite Quantum Dots Incorporated into a Silica/Alumina Monolith. *Angew. Chem.* **2017**, *129*, 8246−8250.

(28) Babu, K. J.; Kaur, G.; Biswal, L.; De, G.; Ghosh, H. N. Ultrafast Charge Delocalization Dynamics of Ambient Stable $CsPbBr_3$ Nanocrystals Encapsulated in Polystyrene Fiber. *Chem.—Eur. J.* **2021**, *27*, 683−691.

(29) Wang, Z.; Fu, R.; Li, F.; Xie, H.; He, P.; Sha, Q.; Tang, Z.; Wang, N.; Zhong, H. One-Step Polymeric Melt Encapsulation Method to Prepare $CsPbBr_3$ Perovskite Quantum Dots/Polymethyl Methacrylate Composite with High Performance. *Adv. Funct. Mater.* **2021**, *31*, No. 2010009.

https://doi.org/10.1021/acsnano.3c11991
ACS Nano 2024, 18, 10054−10062

(30) Jiang, G.; Guhrenz, C.; Kirch, A.; Sonntag, L.; Bauer, C.; Fan, X.; Wang, J.; Reineke, S.; Gaponik, N.; Eychmüller, A. Highly Luminescent and Water-Resistant $CsPbBr_3$ − $CsPb_2Br_5$ Perovskite Nanocrystals Coordinated with Partially Hydrolyzed Poly(Methyl Methacrylate) and Polyethylenimine. *ACS Nano* **2019**, *13*, 10386−10396.
(31) Lv, W.; Li, L.; Xu, M.; Hong, J.; Tang, X.; Xu, L.; Wu, Y.; Zhu, R.; Chen, R.; Huang, W. Improving the Stability of Metal Halide Perovskite Quantum Dots by Encapsulation. *Adv. Mater.* **2019**, *31*, No. 1900682.
(32) Wei, Y.; Cheng, Z.; Lin, J. An Overview on Enhancing the Stability of Lead Halide Perovskite Quantum Dots and Their Applications in Phosphor-Converted LEDs. *Chem. Soc. Rev.* **2019**, *48*, 310−350.
(33) Yoon, H. C.; Lee, S.; Song, J. K.; Yang, H.; Do, Y. R. Efficient and Stable $CsPbBr_3$ Quantum-Dot Powders Passivated and Encapsulated with a Mixed Silicon Nitride and Silicon Oxide Inorganic Polymer Matrix. *ACS Appl. Mater. Interfaces* **2018**, *10*, 11756−11767.
(34) Carulli, F.; He, M.; Cova, F.; Erroi, A.; Li, L.; Brovelli, S. Silica-Encapsulated Perovskite Nanocrystals for X-Ray-Activated Singlet Oxygen Production and Radiotherapy Application. *ACS Energy Lett.* **2023**, *8*, 1795−1802.
(35) Wang, H.-C.; Lin, S.-Y.; Tang, A.-C.; Singh, B. P.; Tong, H.-C.; Chen, C.-Y.; Lee, Y.-C.; Tsai, T.-L.; Liu, R.-S. Mesoporous Silica Particles Integrated with All-Inorganic $CsPbBr_3$ Perovskite Quantum-Dot Nanocomposites (MP-PQDs) with High Stability and Wide Color Gamut Used for Backlight Display. *Angew. Chem., Int. Ed.* **2016**, *55*, 7924−7929.
(36) Li, Z.; Song, C.; Li, J.; Liang, G.; Rao, L.; Yu, S.; Ding, X.; Tang, Y.; Yu, B.; Ou, J.; Lemmer, U.; Gomard, G. Highly Efficient and Water-Stable Lead Halide Perovskite Quantum Dots Using Super-hydrophobic Aerogel Inorganic Matrix for White Light-Emitting Diodes. *Adv. Mater. Technol.* **2020**, *5*, No. 1900941.
(37) Kim, H.; Hight-Huf, N.; Kang, J.; Bisnoff, P.; Sundararajan, S.; Thompson, T.; Barnes, M.; Hayward, R. C.; Emrick, T. Polymer Zwitterions for Stabilization of $CsPbBr_3$ Perovskite Nanoparticles and Nanocomposite Films. *Angew. Chem.* **2020**, *132*, 10894−10898.
(38) Xi, L.; Boothroyd, C. B.; Salim, T.; Borghardt, S.; Lam, Y. M.; Kardynał, B. E. Facile in Situ Synthesis of Stable Luminescent Organic−Inorganic Lead Halide Perovskite Nanoparticles in a Polymer Matrix. *J. Mater. Chem. C* **2017**, *5*, 7207−7214.
(39) Tian, R.; Li, K.; Lin, Y.; Lu, C.; Duan, X. Characterization Techniques of Polymer Aging: From Beginning to End. *Chem. Rev.* **2023**, *123*, 3007−3088.
(40) Hu, Z.; Liu, Z.; Bian, Y.; Li, S.; Tang, X.; Du, J.; Zang, Z.; Zhou, M.; Hu, W.; Tian, Y.; Leng, Y. Enhanced Two-Photon-Pumped Emission from In Situ Synthesized Nonblinking $CsPbBr_3/SiO_2$ Nanocrystals with Excellent Stability. *Adv. Opt. Mater.* **2018**, *6*, No. 1700997.
(41) Xu, L.; Chen, J.; Song, J.; Li, J.; Xue, J.; Dong, Y.; Cai, B.; Shan, Q.; Han, B.; Zeng, H. Double-Protected All-Inorganic Perovskite Nanocrystals by Crystalline Matrix and Silica for Triple-Modal Anti-Counterfeiting Codes. *ACS Appl. Mater. Interfaces* **2017**, *9*, 26556−26564.
(42) Almeida, G.; Goldoni, L.; Akkerman, Q.; Dang, Z.; Khan, A. H.; Marras, S.; Moreels, I.; Manna, L. Role of Acid−Base Equilibria in the Size, Shape, and Phase Control of Cesium Lead Bromide Nanocrystals. *ACS Nano* **2018**, *12*, 1704−1711.
(43) Jeon, S.; Lee, S. Y.; Kim, S.; Kim, W.; Park, T.; Bang, J.; Ahn, J.; Woo, H. K.; Chae, J.; Paik, T.; Seong, T.; Oh, S. J. All-Solution Processed Multicolor Patterning Technique of Perovskite Nanocrystal for Color Pixel Array and Flexible Optoelectronic Devices. *Adv. Opt. Mater.* **2020**, *8*, No. 2000501.
(44) Trinh, C. K.; Lee, H.; So, M. G.; Lee, C.-L. Synthesis of Chemically Stable Ultrathin SiO_2-Coated Core-Shell Perovskite QDs via Modulation of Ligand Binding Energy for All-Solution-Processed Light-Emitting Diodes. *ACS Appl. Mater. Interfaces* **2021**, *13*, 29798−29808.
(45) Zhang, F.; Shi, Z.; Li, S.; Ma, Z.; Li, Y.; Wang, L.; Wu, D.; Tian, Y.; Du, G.; Li, X.; Shan, C. Synergetic Effect of the Surfactant and Silica Coating on the Enhanced Emission and Stability of Perovskite Quantum Dots for Anticounterfeiting. *ACS Appl. Mater. Interfaces* **2019**, *11*, 28013−28022.
(46) Geng, Y.; Guo, J.; Wang, H.; Ling, S. D.; Chen, Z.; Chen, S.; Xu, J. Large-Scale Production of Ligand-Engineered Robust Lead Halide Perovskite Nanocrystals by a Droplet-Based Microreactor System. *Small* **2022**, *18*, No. 2200740.
(47) Sun, C.; Zhang, Y.; Ruan, C.; Yin, C.; Wang, X.; Wang, Y.; Yu, W. W. Efficient and Stable White LEDs with Silica-Coated Inorganic Perovskite Quantum Dots. *Adv. Mater.* **2016**, *28*, 10088−10094.
(48) Luo, B.; Pu, Y.; Lindley, S. A.; Yang, Y.; Lu, L.; Li, Y.; Li, X.; Zhang, J. Z. Organolead Halide Perovskite Nanocrystals: Branched Capping Ligands Control Crystal Size and Stability. *Angew. Chem., Int. Ed.* **2016**, *55*, 8864−8868.
(49) Liang, Y.; Shang, Q.; Li, M.; Zhang, S.; Liu, X.; Zhang, Q. Solvent Recrystallization-Enabled Green Amplified Spontaneous Emissions with an Ultra-Low Threshold from Pinhole-Free Perovskite Films. *Adv. Funct. Mater.* **2021**, *31*, No. 2106108.
(50) Cho, C.; Palatnik, A.; Sudzius, M.; Grodofzig, R.; Nehm, F.; Leo, K. Controlling and Optimizing Amplified Spontaneous Emission in Perovskites. *ACS Appl. Mater. Interfaces* **2020**, *12*, 35242−35249.
(51) Ma, W.; Jiang, T.; Yang, Z.; Zhang, H.; Su, Y.; Chen, Z.; Chen, X.; Ma, Y.; Zhu, W.; Yu, X.; Zhu, H.; Qiu, J.; Liu, X.; Xu, X.; Yang, Y. (Michael). Highly Resolved and Robust Dynamic X-Ray Imaging Using Perovskite Glass-Ceramic Scintillator with Reduced Light Scattering. *Adv. Sci.* **2021**, *8*, No. 2003728.
(52) De Mello, J. C.; Wittmann, H. F.; Friend, R. H. An Improved Experimental Determination of External Photoluminescence Quantum Efficiency. *Adv. Mater.* **1997**, *9*, 230−232.
(53) Chouhan, L.; Ghimire, S.; Biju, V. Blinking Beats Bleaching: The Control of Superoxide Generation by Photo-ionized Perovskite Nanocrystals. *Angew. Chem., Int. Ed.* **2019**, *58*, 4875−4879.
(54) Krieg, F.; Ochsenbein, S. T.; Yakunin, S.; Ten Brinck, S.; Aellen, P.; Süess, A.; Clerc, B.; Guggisberg, D.; Nazarenko, O.; Shynkarenko, Y.; Kumar, S.; Shih, C.-J.; Infante, I.; Kovalenko, M. V. Colloidal $CsPbX_3$ (X = Cl, Br, I) Nanocrystals 2.0: Zwitterionic Capping Ligands for Improved Durability and Stability. *ACS Energy Lett.* **2018**, *3*, 641−646.
(55) Qiu, L.; Yang, H.; Dai, Z.; Sun, F.; Hao, J.; Guan, M.; Dang, P.; Yan, C.; Lin, J.; Li, G. Highly Efficient and Stable $CsPbBr_3$ Perovskite Quantum Dots by Encapsulation in Dual-Shell Hollow Silica Spheres for WLEDs. *Inorg. Chem. Front.* **2020**, *7*, 2060−2071.
(56) Li, J.; Li, Z.; Qiu, J.; Li, J. Photothermal Optimization of Quantum Dot Converters for High-Power Solid-State Light Sources. *Adv. Opt. Mater.* **2022**, *10*, No. 2102201.
(57) Wang, X.; Wang, Y.; Wang, Y.; Liu, H.; Zhang, Y.; Liu, W.; Wang, X.; Wang, S. Color-Tunable X-Ray Scintillation Based on a Series of Isotypic Lanthanide−Organic Frameworks. *Chem. Commun.* **2020**, *56*, 233−236.
(58) Zhao, W.; Wang, Y.; Guo, Y.; Suh, Y. D.; Liu, X. Color-Tunable and Stable Copper Iodide Cluster Scintillators for Efficient X-Ray Imaging. *Adv. Sci.* **2023**, *10*, No. 2205526.

https://doi.org/10.1021/acsnano.3c11991
ACS Nano 2024, 18, 10054−10062